210524

International Journal of Remote Sensing res103378.3d 27/11/06 19:34:44
The Charlesworth Group, Wakefield +44(0)1924 369598 - Rev 7.51n/W (Jan 20 2003)

Authors Queries

Journal: **International Journal of Remote Sensing**
Paper: **210524**
Title: **Orthorectified image mosaic of Antarctica from 1963 Argon satellite photography: image processing and glaciological applications**

Dear Author
During the preparation of your manuscript for publication, the questions listed below have arisen. Please attend to these matters and return this form with your proof. Many thanks for your assistance

Query Reference	Query	Remarks
1	In equation (1), can the authors please change 'dXt', 'dYt' and 'dZt' to 'dXt', 'dYt', 'dZt' (i.e. 'd' should not be in italics). Also, what is the meaning/definition of 'N'?	
2	In table 1, what is '(m)'? If it is a unit (i.e. metre), then it should not be a subscript.	
3	In table 1, what is '(m)'? If it is a unit (i.e. metre), then it should not be a subscript.	
4	In table 2, what are the units of the 'Distance' column?	
5	In table 2, what are the units of the 'Distance' column?	
6	In table 3, what are the units of the 'velocities'?	
7	In table 3, what are the units of the 'velocities'?	
8	Is there a reference available for this 'second paper'?	
9	Do the authors wish to have an 'Acknowledgments' section?	

International Journal of Remote Sensing
Vol. 000, No. 000, 0 Month 2006, 1–17

Orthorectified image mosaic of Antarctica from 1963 Argon satellite photography: image processing and glaciological applications

K. KIM*†, K. C. JEZEK‡ and H. LIU§
†Microsoft Corporation, Boulder, Colorado 80301, USA
‡Byrd Polar Research Center, The Ohio State University, Columbus, Ohio 43210, USA
§Department of Geography, Texas A&M University, College Station, Texas 77843, USA

(*Received 26 August 2005; in final form 6 November 2006*)

Using the state-of-art digital imaging technology, extended block adjustment, orthorectification and mosaicking, individual Declassified Intelligence Satellite Argon photographic images are precisely assembled into a map quality mosaic of coastal Antarctica. The geometric accuracy of the mosaic is estimated to be approximately equivalent to the original resolution of the Argon photography, which is about 140 m. We compare the Argon mosaic with later satellite images to investigate changes in ice sheet geographic features and dynamical glaciological processes.

1. Introduction

Prior to satellite observations, Antarctica remained one of the most poorly mapped parts of our planet. Since the early 1970s, remotely sensed data provided opportunities to overcome challenging environmental obstacles so as to conduct large-scale analysis of the Antarctic ice sheet and its coastal environs. An extensive collection of early 1970s Landsat 1, 2 and 3 Multi-Spectral Scanner (MSS) images was the first impetus to map the Antarctic from space (Swithinbank 1973, Swithinbank and Luchitta 1986). The maps were later compared to late 1980s and early 1990s Landsat 4 and 5 MSS and Thematic Mapper (TM) images, and 1992 and 1995 European Space Agency's Earth Remote-Sensing Satellite radar images (Williams *et al*. 1995) for change detection studies. The moderate spatial resolution (1 to 2.5 km) and wide swath (2400 km) of Advanced Very High Resolution Radiometer (AVHRR) images helped reveal details about ice stream flow in West Antarctica (Bindschadler 1998). After the original AVHRR mosaic of Antarctica (Merson 1989), the United State Geological Survey (USGS) made subsequent improvements to the mosaic by eliminating more cloud, separating the thermal band information to illustrate surface features more clearly, and correcting the coastline of the mosaic to include grounded ice while excluding thin, floating fast ice (Ferrigno *et al*. 1996). In 1997, Radarsat-1 Synthetic Aperture Radar (SAR) data was successfully acquired over the entirety of Antarctica. The coverage is complete and was used to create the first, high-resolution (25 m) radar image mosaic of Antarctica (Jezek 1999).

Before 1995, scientists were restricted to airborne data as a source for high-resolution broad-scale coverage for the era preceding Landsat. More extensive

*Corresponding author. Email: keekim@microsoft.com

International Journal of Remote Sensing
ISSN 0143-1161 print/ISSN 1366-5901 online
http://www.tandf.co.uk/journals
DOI: 10.1080/01431160601105850

spaceborne coverage at high-resolution became available through the declassification of early satellite reconnaissance photographs (McDonald 1995, Peebles 1997, Wheelon 1997). These are known as Declassified Intelligence Satellite Photographs (DISP), which were taken by a series of reconnaissance satellites called Corona, Lanyard, and Argon, launched in the early 1960s in polar orbits. The Antarctic data was collected as part of the Argon program, which operated between 1961 and 1964.

The DISP data is an invaluable resource for studying the Antarctic. Bindschadler and Vornberger (1998) and Jezek (1998) compared Argon images with more recent data (e.g. AVHRR, SPOT and SAR) to examine how different Antarctic flow regimes have changed at decadal intervals. The authors used a two-dimensional linear wrapping function to match it to other data, but the accuracy of the co-registration is not sufficient to reliably measure changes, because of nonlinear distortions arising from earth curvature effects.

Kim *et al.* (2001) compiled Argon images along the coast of Queen Maud Land into a mosaic. Comparison with 1997 Radarsat imagery showed that the ice shelves in this region lost about 6.8% of their total area with most of the retreat occurring between 1963 and the mid-1970s. To overcome registration errors, they proposed a simple, rigorous method for the geometric processing of Argon images based on space resection. Space resection is the process of obtaining the sensor position and attitude information of the perspective centre (e.g. exterior orientation parameters) in relation to ground control points (GCPs). This method is limited when mapping multiple images because each image is processed individually, with a minimum of three GCPs required for each image, and, frequently the number of reliable GCPs is limited. In addition, individual frame processing does not use the internal relationships between adjacent images in a block to minimize and distribute the errors commonly associated with GCPs, image measurements, digital elevation models and sensor information. Therefore, misalignment between adjacent processed images is likely since the error has not been minimized and distributed throughout the block.

Zhou *et al.* (2002) proposed a simultaneous block triangulation to map Greenland using 24 Argon images acquired in 1962 and 36 Argon images acquired in 1963. The main idea of this approach is to connect the images in a block using tie points (TPs), so that the entire image set can be processed as one large image block with a sparse set of GCPs. The errors caused by misalignment between adjacent processed images can also be minimized. They assumed that the GCPs were error-free, i.e. the uncertainties of GCPs were not taken into account in the adjustment process. They compared the map to the 1992 ERS Synthetic Aperture Radar map of Greenland (Fahnestock *et al.* 1993) and estimated the relative accuracy to be 200 m and the absolute accuracy to be about 450 m. Zhou and Jezek (2002) used the resulting mosaics to map ice margins, flow stripes, and shear margins in an investigation of variability in Greenlandic outlet glaciers and ice streams.

In this paper, we describe a map of the Antarctic coastal margin compiled from 62 Argon photographs acquired between 29 August and 3 November 1963. We apply an extended block adjustment with constraints on the stochastic properties of GCPs as described by Koch (1998) and the American Society of Photogrammetry (1980). Essentially, the extended block adjustment takes into account errors in the coordinates of the GCPs when estimating the unknown exterior orientation parameters (EOP). We compare the 1963 mosaic with the 1997 SAR mosaic and

210524
International Journal of Remote Sensing res103378.3d 27/11/06 19:34:48
The Charlesworth Group, Wakefield +44(0)1924 369598 - Rev 7.51n/W (Jan 20 2003)

illustrate how data from the two sets of observations can be used to detect changes in ice sheet geographical boundaries and to measure long-term average ice sheet velocity.

2. Argon imagery

The Argon 9058A and 9059A missions were launched on 29 August 1963 and 29 October 1963 respectively. They each carried a single, vertically oriented, panchromatic frame camera with a 76.2 mm focal length. The satellites flew at an altitude of 322 km and in an orbit that allowed imaging to the pole. Individual images cover approximately 540×540 km with overlap between adjacent scenes (McDonald 1995). Corner points provided in the metadata and derived from the legacy ephemeris data are estimated to be accurate to about 16 km. There is no specific radiometric calibration information or ancillary imaging information, such as sun zenith angle, provided in the metadata associated with the individual photographs as distributed by the US Geological Survey (http://edc.usgs.gov/products/satellite/declass1.html).

The Argon photographs are preserved on black and white photographic film transparencies (11.4×11.4 cm). Film resolution is 30 lines per mm, and the corresponding spatial resolution (i.e. pixel equivalent) is approximately 140 m. The Argon film transparencies were digitally scanned at 7 μm using the INTERGRAPH PhotoScan TD® Scanner, which is a high-resolution radiometrically and geometrically precise flatbed scanning system.

Based on visual inspection of the browse images available on the Earth Resources Observation Systems (EROS) Data Center, an optimal dataset of 62 Argon photographs was identified that covered the entire Antarctic coast (figure 1). Frames were selected from the first 47 revolutions of the 9058A mission and from the first 76 revolutions of the 9059A mission. The outline of the Antarctic continent with the location of each frame is shown in figure 1. The locations of all of the Antarctic photos collected during the Argon mission are described by Bindschadler and Seider (1998). Compilation of the entire Antarctic dataset into an orthorectified image mosaic is limited by the lack of control on the nearly featureless interior photos, and consequently we concentrated on the margins.

3. Geometric control data

Radarsat-1 SAR data was acquired over Antarctica between 19 September and 14 October 1997. The coverage is complete and was used to construct a seamless image mosaic of Antarctica. The SAR data was orthorectified using the 200 m grid Ohio State University (OSU) Antarctic Digital Elevation Model (DEM) (Liu *et al.* 1999). The elevation model was created by integrating cartographic and remotely sensed data. The accuracy of the DEM is estimated at about 130 m over rugged mountainous areas, better than 2 m for the ice shelves, better than 15 m for the interior ice sheet and about 35 m for the steeper ice sheet perimeter (Liu *et al.* 1999). The OSU Antarctic DEM was also used for terrain correction of the Argon photographs.

We used a 100 m resolution Radarsat-1 SAR image mosaic for horizontal control and the 200 m grid OSU Antarctic DEM for vertical control. The horizontal geolocation accuracy of the SAR mosaic over ice-covered terrain was estimated to be approximately 100 m (Noltimier *et al.* 1999), and the vertical accuracy of the

210524
International Journal of Remote Sensing res103378.3d 27/11/06 19:34:48
The Charlesworth Group, Wakefield +44(0)1924 369598 - Rev 7.51n/W (Jan 20 2003)

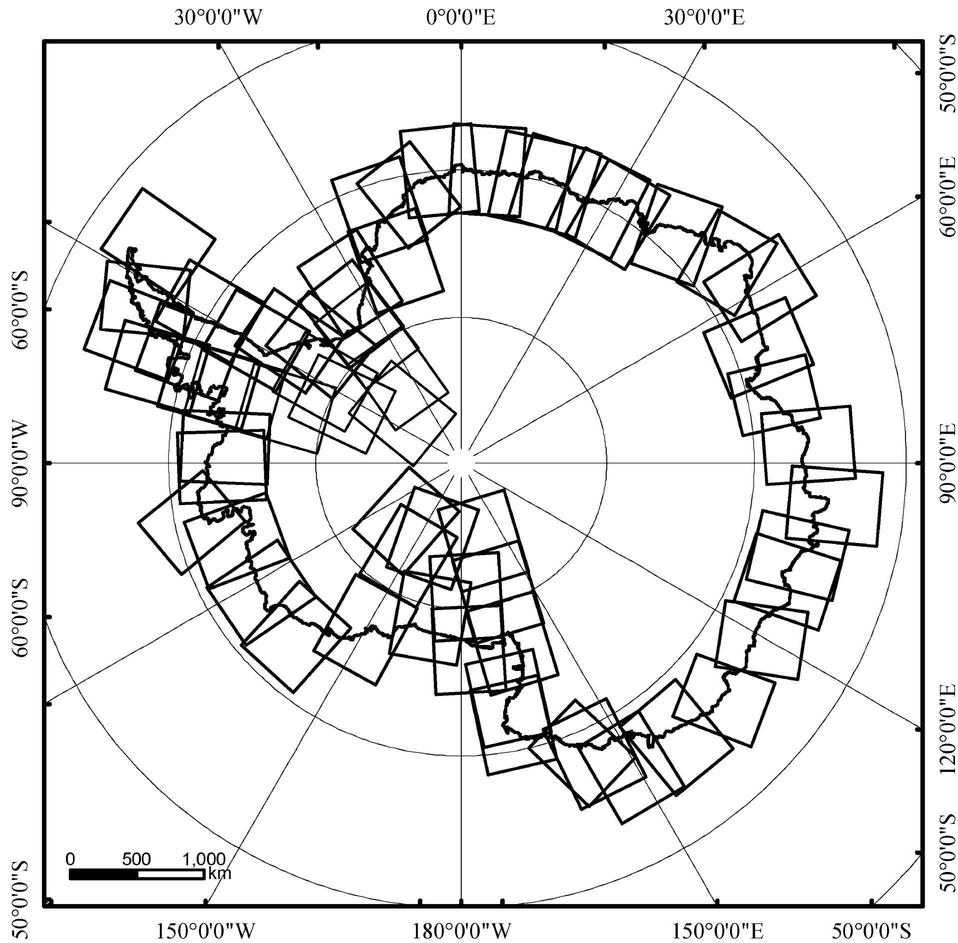

Figure 1. Outline of coastal Antarctica with location of 62 Argon frames. The map uses a polar stereographic projection with a standard parallel of $-71°$ S on a WGS84 ellipsoid.

DEM was estimated to be approximately 35 m for the Antarctic coast (Liu *et al.* 1999). Figure 2 shows image chips of GCPs (e.g. common points) with known image (Argon) and object (SAR) coordinates. The GCPs were selected on exposed rock areas that can be easily identified in the SAR and Argon images.

4. Orthorectification and mosaicking

Argon satellite photographs were captured with overlap areas. This was advantageous and allowed us to use a block adjustment, which can incorporate the minimum number of GCPs distributed across several overlapping scenes. This method was especially important for processing the image data over Antarctica where cloud cover can obscure large sectors of an intermediate image. Figure 3 shows an example of a block model with five Argon images taken over the Antarctic Peninsula. Twelve TPs and seventeen GCPs were selected to tie images and determine the exterior orientation parameters (e.g. three positions and three attitudes) of each image in the block. The horizontal coordinates of the GCPs were

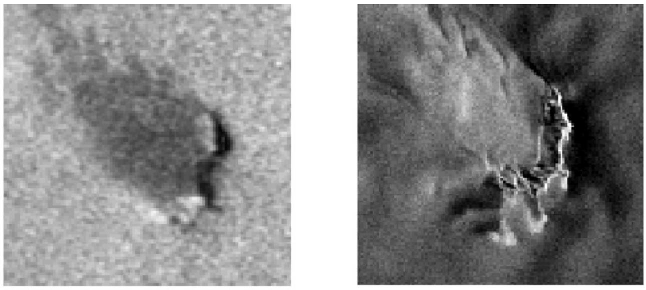

(*a*) (*b*)

Figure 2. Image chips of the observed GCPs with known (*a*) image (Argon) and (*b*) object (SAR) coordinates.

determined by identifying common features in the orthorectified Radarsat-1 SAR image mosaic. The corresponding elevations were taken from the OSU Antarctic DEM. The uncertainty of the measured image coordinates was estimated to be 14 μm (two pixels). The uncertainties of the observed GCPs were estimated to be 100 m from the Radarsat-1 SAR mosaic and 35 m from the OSU Antarctic DEM, and were weighted inversely proportional to the uncertainty values, so that points with high errors affected the solution less than points with lower errors.

The mathematical model is similar in concept to the block adjustment of the photogrammetric collinearity equations that establish a convenient relationship between image and object spaces by enforcing the condition that the perspective centre, a point in object space and its image are on a straight line. In this paper, we skip the details of deriving the block adjustment model and refer the interested reader to Zhou *et al.* (2002) and Kim (2004). Instead, we focus on discussing how the block adjustment can be extended to the case of the uncertainties of the observed GCPs.

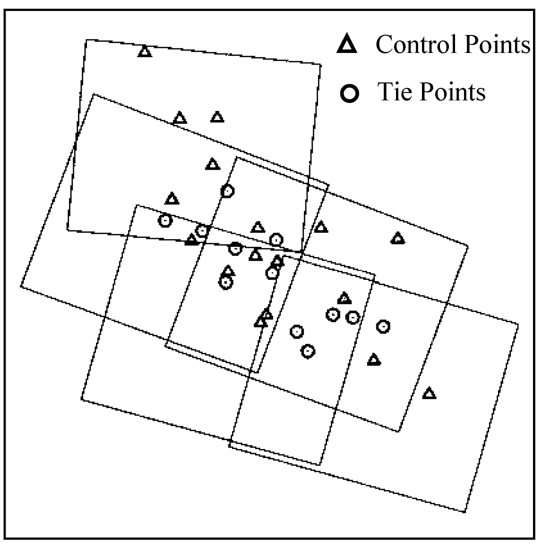

Figure 3. A block model with 12 TPs (circles) and 17 GCPs (triangles).

The accuracy of the observed GCPs may not always be good enough for a mapping application in which the GCPs are measured from a small-scale (or coarse resolution) map. In our case, the GCPs were obtained from a 100 m resolution image mosaic and 200 m grid DEM, namely, the uncertainties of the given GCPs must be considered as additional unknown parameters to be adjusted during the block adjustment process. These uncertainties can be taken into account in the adjustment process (American Society of Photogrammetry 1980, Koch 1998). We applied an extended block adjustment with additional constraints based on the stochastic properties of GCPs as described by Koch (1998) and the American Society of Photogrammetry (1980). Essentially, we took into account errors in the object coordinates of the GCPs when estimating the unknown exterior orientation parameters (EOP). The object coordinates were the given three-dimensional Cartesian coordinates of the observed GCPs. The mathematical model for the uncertainties of the object coordinates of the GCPs is given by:

$$\begin{bmatrix} X - X_t^0 \\ Y - Y_t^0 \\ Z - Z_t^0 \end{bmatrix} = \begin{bmatrix} \mathrm{d}X_t \\ \mathrm{d}Y_t \\ \mathrm{d}Z_t \end{bmatrix} + \underline{e}_2 \quad \underline{e}_2 \sim N\left(0, \sigma_{0_2}^2, p_2^{-1}\right), \tag{1}$$

where X, Y and Z were the object coordinates of the given GCPs; X_t^0, Y_t^0 and Z_t^0 were the initial values for the refined GCPs; $\mathrm{d}X_t$, $\mathrm{d}Y_t$ and $\mathrm{d}Z_t$ were the differences between the values of the refined and initially prescribed GCPs; $\underline{e}_2$ was the noise vector contaminating X, Y and Z; $\sigma_{0_2}^2$ was the variance component of the observations; and p_2 was the weight matrix of the observations.

It is important to note that the left-hand side of equation (1) was numerically zero plus some uncertainties for using the given GCP coordinates themselves as initial values. The effect of the errors in the coordinates of the GCPs, however, smeared into the block adjustment process and affected the estimates of the unknown parameters.

We combined the traditional error-free GCP collinearity adjustment equation (e.g. $y_1 = A_1\xi_1 + e_1$) with the new GCP error model in equation (1) to create equation (2) that sets up extended observation equations for the block adjustment with constraints from the stochastic properties of the GCPs as follows:

$$\begin{bmatrix} y_1 \\ y_2 \end{bmatrix} = \begin{bmatrix} A_1 & A_2 \\ 0 & I \end{bmatrix} \begin{bmatrix} \xi_1 \\ \xi_2 \end{bmatrix} + \begin{bmatrix} \underline{e}_1 \\ \underline{e}_2 \end{bmatrix}. \tag{2}$$

y_1 was the given difference between the observed and initial image coordinates of the EOPs and TPs; y_2 was the given difference between the observed and initial object coordinates of the GCPs; ξ_1 was the estimated EOP and TP update from the previous iteration process in the object coordinates; ξ_2 was the estimated GCP update from the previous iteration process in the object coordinates, i.e. $\mathrm{d}X_t$, $\mathrm{d}Y_t$ and $\mathrm{d}Z_t$ in equation (1); A_1 was the matrix of the partial derivatives related to the EOPs; A_2 was the matrix of the partial derivatives related to the TPs; I was an identity matrix; and $\underline{e}_1$ and $\underline{e}_2$ were the noise vectors contaminating y_1 and y_2 respectively.

We estimated the unknown parameters, ξ_1 and ξ_2 by inverting equation (2) by a least-square adjustment.

The EOPs estimated by the extended block adjustment and the OSU Antarctic DEM were used to perform the image orthorectification that eliminates topographic relief displacement inherent within Argon imagery. The orthorectification process was performed image-by-image using the following procedures. First, an orthorectified image grid with a desired resolution (e.g. 100 m) and a map projection (e.g. polar stereographic) was defined by calculating the minimum and maximum map coordinates in the block. Second, for each grid location of the orthorectified image, the corresponding DEM value was taken and its equivalent pixel positions in the original image were computed using the collinearity equations. A brightness value was determined for this image pixel location using bilinear resampling of the surrounding pixels. It is important to note that the map projection process combines with the orthorectification process because the original image needs to be resampled by only once. Finally, 100 m orthorectified Argon images were produced in polar stereographic projection with a standard parallel of 71° S on a WGS84 ellipsoid.

We combined the orthorectified images into a single composite mosaic. In practice, we observed significant image-to-image radiometric variations that were mainly due to changes in atmospheric transmittance and in illumination caused by different sun angles and varying degrees of cloud cover. To overcome this problem, we used a two-step mosaic process. First, we visually checked the image histograms and performed a linear stretch so that the peaks of the image histograms were similarly located with all values in between getting stretched proportionally. Second, a simple minimum difference algorithm was used to identify pixels that have minimum difference values in the overlap area. The identified pixels were then used as a cutline to determine which sections of the individual images will be placed into the final mosaic. Similarly, block to block radiometric adjustments were applied to smooth the boundaries between blocks. However, some radiometric effects on the interiors of the frames still exist in figure 5 later on because the linear stretch was mainly focused on smoothing the boundaries, which is important for our application

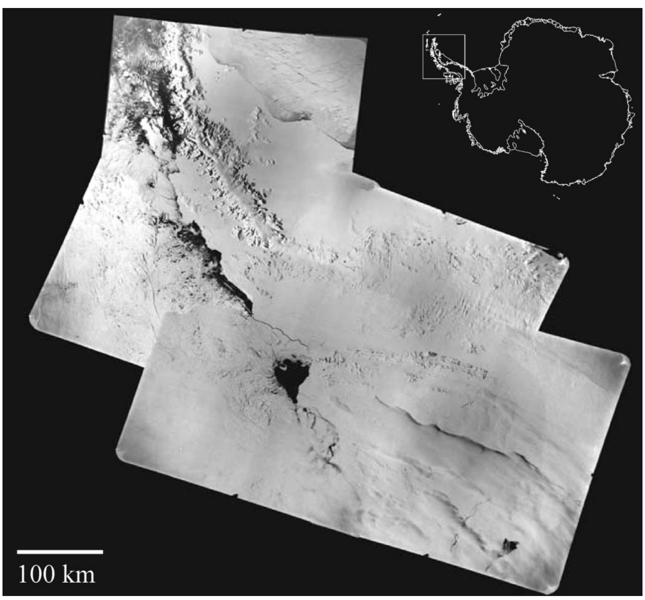

Figure 4. The 100 m orthorectified image mosaic of the Antarctic Peninsula in polar stereographic projection with 71° S standard parallel on a WGS84 ellipsoid.

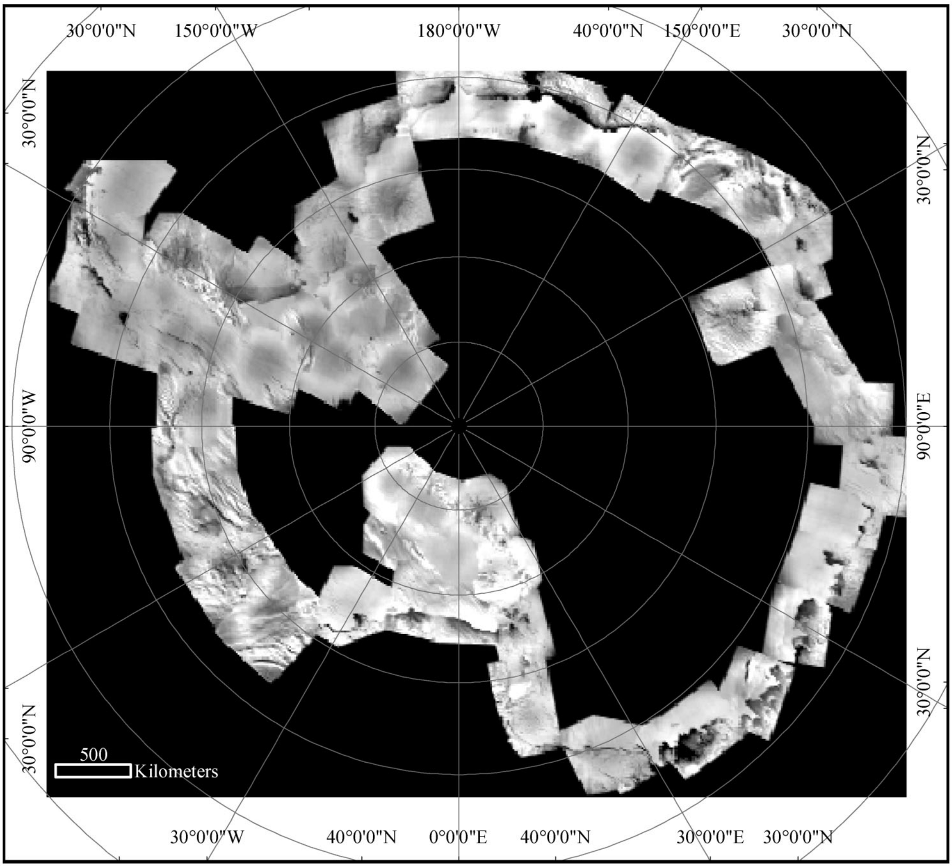

Figure 5. The 1963 Argon Antarctic mosaic complied from 62 orthorectified images in polar stereographic projection with a standard parallel of 71° S on a WGS84 ellipsoid.

of coastline mapping where a smooth radiometric transition facilitates boundary mapping, whereas an abrupt transition will confuse the algorithm. Figure 4 shows the image block containing the Antarctic Peninsula.

The geolocation consistency of the mosaic was estimated to be less than two pixels (e.g. 200 m) by computing the differences between the original GCP locations and the GCP locations transformed by the estimated EOP and DEM values. In addition, Kim *et al.* (2001) assessed the relative errors by measuring common points on the final orthorectified Argon and SAR mosaics to check independently the relative accuracy of the orthorectified Argon mosaic. They found that the relative accuracy was about 120 m. Regarding the absolute accuracy, the reference SAR mosaic has been independently evaluated for geometric fidelity by Ferrigno *et al.* (2005) who concluded that a geolocation accuracy of 150 m was reasonable in near coastal areas, but could be worse in mountainous area where there was less control.

Fifteen blocks were processed by the extended block adjustment, orthorectification and mosaicking. Each block consisted of two to five images, depending on the cloud cover and the distribution of the GCPs in the block. The accuracy of the points obtained from a block process depends primarily on the number of images bridged between the GCPs, i.e. it is a common practice not to bridge more than five

Table 1. Horizontal positional accuracies of each orthorectified image block.

				σ_{x} (m)		σ_{y} (m)		σ(m)	
Blocks	Photos	CPs	TPs	CP	TP	CP	TP	CP	TP
1	4	17	9	104.94	139.18	127.07	122.32	164.80	185.29
2	2	8	3	93.22	188.24	148.62	181.64	175.43	261.58
3	3	6	6	163.49	166.63	61.53	47.52	174.62	173.27
4	3	7	6	15.99	85.05	10.13	32.06	18.92	90.89
5	3	7	7	100.02	144.40	56.53	126.40	114.88	191.90
6	5	17	9	50.05	141.23	147.68	82.64	155.93	163.63
7	2	8	3	154.41	58.92	167.79	184.32	228.02	193.50
8	4	14	9	111.17	190.13	91.40	184.88	143.91	265.19
9	4	18	7	161.31	89.09	178.86	82.20	240.85	121.21
10	3	10	5	120.75	111.21	84.35	130.23	147.29	171.25
11	2	7	3	50.35	167.97	111.93	125.58	122.73	209.72
12	4	14	8	121.58	107.15	84.83	170.93	148.24	201.73
13	4	17	11	138.35	149.44	154.41	142.21	207.32	206.29
14	4	10	12	112.30	128.51	52.70	123.84	124.05	178.46
15	5	17	12	104.73	123.82	60.27	144.86	120.83	190.56

images to be considered in a strip block (Kraus 1993). Table 1 shows a summary of each orthorectified image block with its error statistics. Because we incorporated estimates of absolute GCP errors in the calculation, the error statistics reported in table 1 are a better estimate of the absolute block errors than would be obtained if we simply applied the error free collinearity equations, which only give the errors relative to the reference map. The sigma values represent the standard deviations of the GCPs used. Figure 5 shows a seamless, orthorectified Argon image mosaic of the entire Antarctic coast. The mosaic was generated by simply assembling all the processed blocks into a common coordinate system with the radiometric correction using the minimum difference algorithm described above. Visual inspection of the seams between blocks did not reveal any offsets greater than one pixel (figure 6). Consequently, no further block to block geometric adjustment was performed. It is a view of the Antarctic coast that graphically depicts intricate coastal properties as they were in 1963.

5. Discussion

In this section, we show several enlargements of regions where the mosaic captures important glaciological processes and events (see location indexes in figure 5). We compare and contrast the Argon vignettes with later satellite imagery and illustrate how the map can be used for glaciological studies of Antarctica.

5.1 *Retreat of the northern Larsen Ice Shelf*

Figure 7 shows an enlargement of the northern Larsen Ice Shelf, which is located near the tip of the Antarctic Peninsula. Our image shows the 1963 ice shelf margin and the sea ice covered waters of the Weddell Sea. Tonal variations on the sea ice may be related to differences in ice age and/or snow thickness. In January 1995, a large area of ice shelf disintegrated into small icebergs during a storm (Rott *et al*. 1996). Skvarca *et al*. (1998) suggested that this rapid collapse coincided with a period of significant climate warming in the Antarctic Peninsula regions. The Larsen Ice Shelf continues to retreat as illustrated by the 1997 Radarsat image shown on the

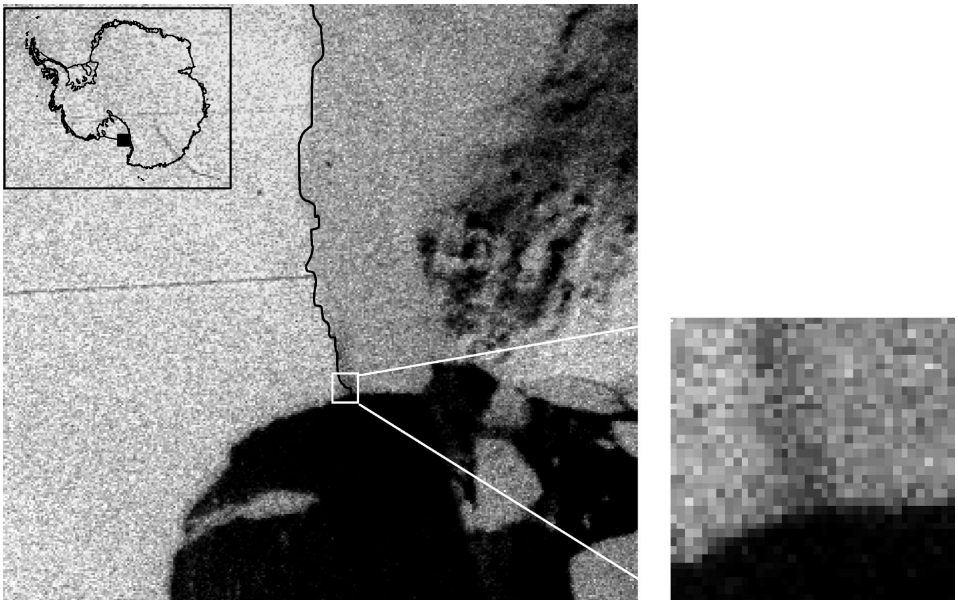

Figure 6. Geometric and radiometric offsets between two orthorectified image blocks. A black seamline for the mosaic is overlaid on the left image to illustrate the boundary. The left side of the image is the Ross Ice Shelf, the right most portion is Cape Crozier, located on Ross Island, and the dark bottom right is either open ocean or very thin sea ice. The enlargement on the right side shows the pixel level registration along the block seam line.

right of figure 7. The area once filled by ice shelf is now filled by darker sea ice. The time series observations provide critical benchmarks for gauging ice shelf retreat, as well as for understanding the mechanisms that precipitate rapid collapse (Scambos *et al*. 2000, Jezek and Liu 2005).

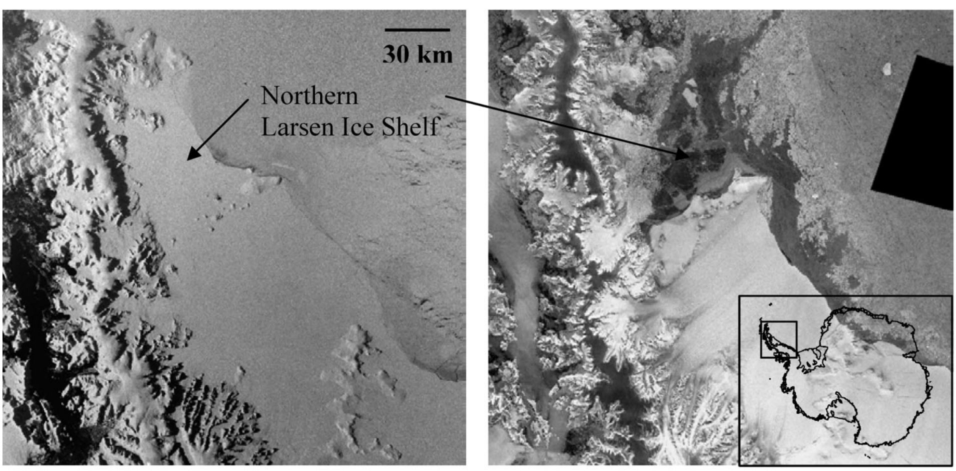

Figure 7. Comparison of 1963 Argon (left) and 1997 Radarsat-1 SAR (right) images of the northern Larsen Ice Shelf. The northern portion of the Larsen Ice Shelf shown as a relatively bright and smooth area in the Argon image is replaced by open water and thin sea ice in the Radarsat image. The retreat of the ice shelf has since extended southward.

5.2 *Flow patterns on the Whillans Ice Stream*

Ice streams are the most dynamic glaciological processes operating in the Antarctic Ice Sheet. Recent evidence shows that the velocity and mass balance of the West Antarctic Ice Streams are changing on decadal time scales (Joughin and Tulaczyk 2002). The tributaries and main trunk of the Whillans Ice Stream are easily observable in Argon imagery (see figure 8). Crevassed areas appear dark in the Argon image because of shadowing. They appear bright in the Radarsat image because they act as corner reflectors. Subtle changes in surface topography also appear in the images because of slight changes in slope. Stearns (2002) analysed directional features interpreted as flow stripes and shear margins on both the 1963 Argon and 1997 Radarsat-1 mosaics. While an analysis of ice margin fluctuations was inconclusive, she found that the 1963 and 1997 flow stripe patterns tend to intersect as the two tributaries merge. Stearns argues that the pattern argues for a

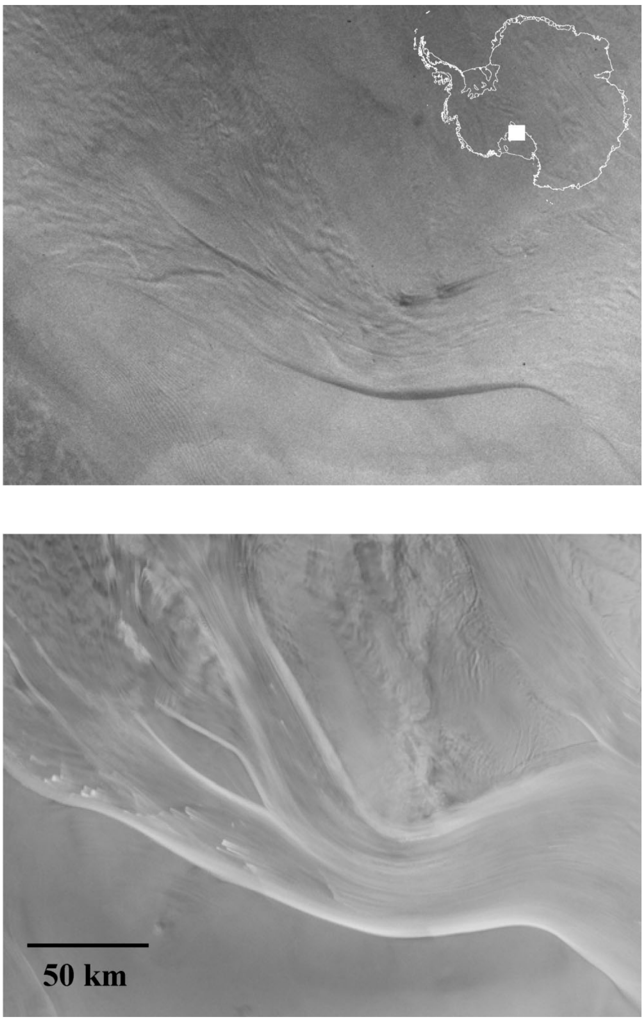

Figure 8. Comparison of 1963 Argon (above) and 1997 Radarsat-1 SAR (below) images of Whillans Ice Stream. The main trunk of the ice stream is seen in the lower right of each image. It is fed by two tributaries separated by an island of more stagnant ice.

reversal in the discharge rates between the two ice streams over the observation period that is consistent with reported changes in flow speed, flow dynamics, and mass balance (Stearns *et al.* 2005).

5.3 *Ice margin fluctuations of the Pine Island Glacier*

The Pine Island Glacier shown in figure 9 was selected for a detailed, local study of ice margin fluctuations. This glacier is one of the largest glaciers in West Antarctica. The glacier speed increased by 18 ± 2 % between 1992 and 2000 (Rignot 2002), and the basin feeding the glacier thinned at $11.7 \pm 1.0\,\mathrm{cm\,yr^{-1}}$ between 1992 and 1996 (Wingham *et al.* 1998). The thinning rate near the grounding line was estimated at $1.6 \pm 0.2\,\mathrm{m\,yr^{-1}}$ between 1992 and 1999 (Shepherd *et al.* 2001). This region is believed to be susceptible to ice sheet collapse (Bentley 1997, Bindschadler 1998), and therefore the evolution of this glacier is of great interest to scientific community.

The 1963 Argon (100 m resolution), 1975 Corona (25 m resolution), 1997 and 2000 Radarsat-1 SAR (25 m resolution), and 2003 ASTER (Advanced Spaceborne Thermal Emission and Reflection Radiometer, 15 m resolution) data was used in this study. Coastline and glacier terminus positions are shown in figure 9 and table 2 respectively. Over the 40 years of observations, we found that the ice margin positions along the middle of the ice streams oscillated between 1.5 and −9.3 km (see table 2 for 1963). These oscillations were mainly due to large calving events that

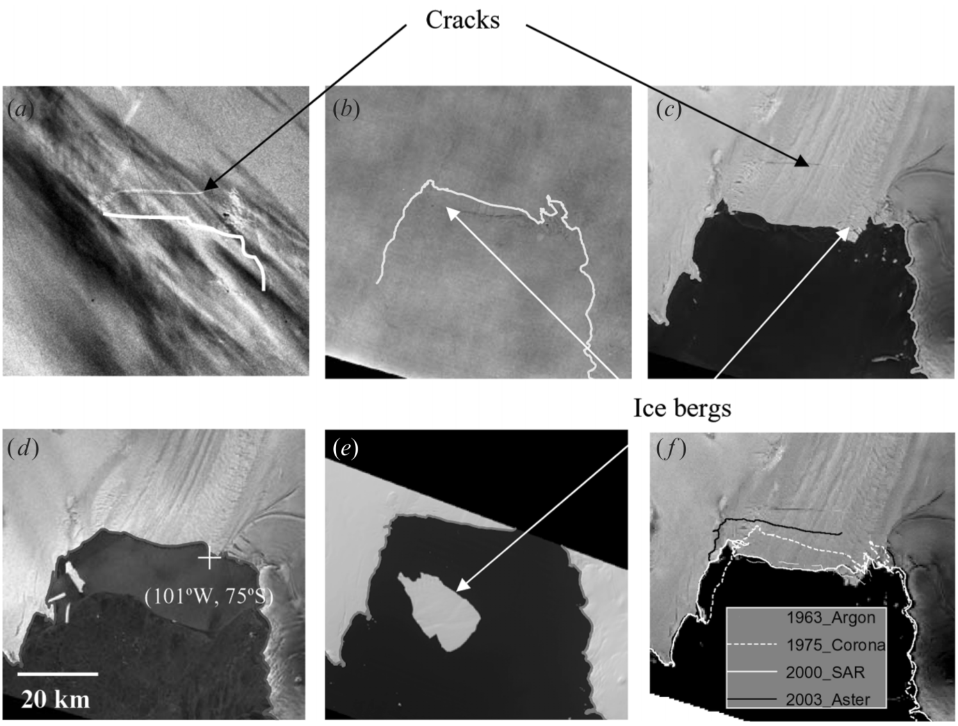

Figure 9. Observations of coastline positions of Pine Island Glacier from: (*a*) 1963 Argon, (*b*) 1975 Corona, (*c*) 1997 Radarsat-1 SAR, (*d*) 2000 Radarsat-1 SAR, (*e*) 2003 ASTER, and (*f*) four observations overlaid on the 1997 SAR image. White lines in (*a*) and (*b*) are interpreted as coastline positions.

Table 2. Pine Island Glacier terminus changes along the middle of the glacier in figure 9 5

Year	Longitudes (°)	Latitudes (°)	Changes	
1963	−101.4800	−74.9319	Distance	Period
1975	−101.6325	−74.9219	−4555.35	1963–1975
1997	−101.6408	−74.9213	1488.49	1963–1997
2000	−101.7944	−74.9113	−4800.24	1963–2000
2003	−101.8444	−74.9080	−9324.56	1963–2003

occurred between 1963 and 2003. In addition, we observed that Pine Island Bay was filled with mixtures of pack ice and fast ice until 1975.

We have noted above that some ice shelves in Antarctica can catastrophically retreat (e.g. the Larsen Ice Shelf in figure 7). Ice shelves that appear to have stable terminus positions can disintegrate over a period of days to weeks. While other scientists have observed large changes in the thinning rate, increasing velocity, and retreating grounding line of the Pine Island Glacier, we observed little change in the glacier terminus positions. This leads us to speculate that the glacier terminus change is not always a good indicator of the glacier health. Moreover, it seems that the calving rate of the Pine Island Glacier (determined by the difference between the forward advance of the ice margin and the upstream ice velocity) must be changing almost synchronously with the glacier velocity, so that the change of the glacier terminus position is small.

5.4 *Surface velocity on the Filchner Ice Shelf*

Time series satellite images provide a direct way to measure ice sheet surface velocity (Luchitta and Ferguson 1986). Essentially, common features are compared on two map projected images and the displacements are measured. Figure 10 shows examples of the Argon and Radarsat-1 SAR mosaics over the Filchner Ice Shelf in Antarctica. Each shows distinctive flow and crevasse features in the ice shelf downstream. The difference in the seaward margin of the ice shelf represents the

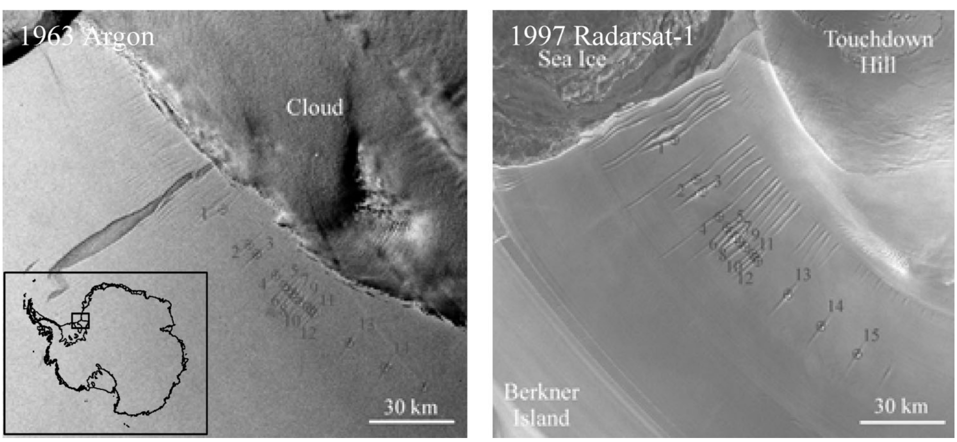

Figure 10. Fifteen ice crevasses identified and measured on the Filchner Ice Shelf. The Grand Chasms area is noticeable on the left centre of the Argon image. Ice north of the Grand Chasms calved in 1986.

consequences of a massive calving event. Somewhat surprisingly, the same crevasses and rifts can be identified on both images. Consequently, 15 common points on individual crevasses were visually identified and geolocated on each image. The displacements were used to compute 34-year-average surface velocities. The computed velocities were compared with 1997 InSAR velocities (see figure 11 and table 3) estimated by Gray *et al*. (1998). The velocities compare favourably point by point and in the overall average, given that the error in both velocity measurements is about 10 m yr^{-1}. There is a slight increase in the InSAR velocity above the average velocity near the calving front. Perhaps this is related to the 1986 Grand Chasms calving event (Ferrigno and Gould 1987), but the generally favourable comparison between those average velocities and the 1997 instantaneous velocities suggests that the large calving event had a small effect on the ice shelf dynamics. Presumably, this is because the ice calved downstream of the flow-controlling bottleneck between Berkner Island and the westward extension of Coats Land.

6. Conclusions

By using the state-of-art digital imaging technology, extended block adjustment using ground control features, orthorectification with a digital elevation model, and mosaicking, we produced an image mosaic of the Antarctic coastal margin as it was in 1963. An extended block adjustment technique with constraints of the stochastic properties of the GCPs allowed us to determine positions of features in object space

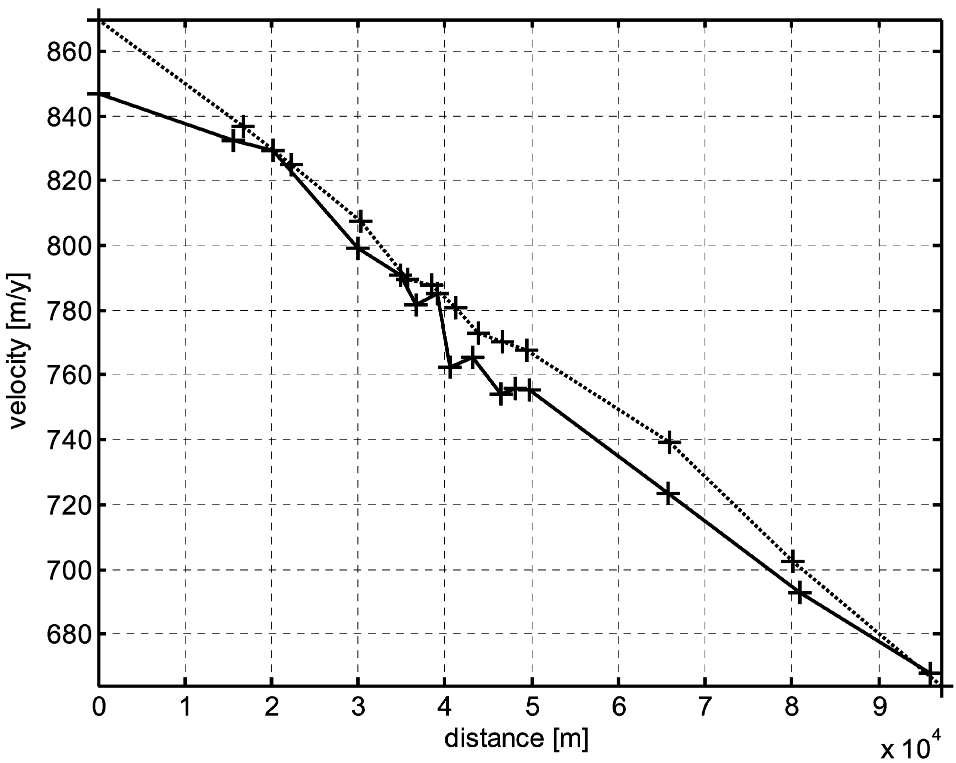

Figure 11. Comparison of 1963 Argon (solid line) and 1997 InSAR (dashed line) velocities on the Filchner Ice Shelf; distances were calculated from the Argon Point 1 in figure 10. Speed errors are about 10 m y^{-1} for each data set.

Table 3. Comparison of Argon and InSAR velocities on the Filchner Ice Shelf in polar stereographic map projection with a 71° S standard parallel on a WGS84 ellipsoid. 7

Points	Argon_x	Argon_y	Argon_vel	Insar_x	Insar_y	Insar_vel
15	−697667	904019	667.8	−697165	903437	664.1
14	−711063	911713	692.6	−711909	912706	702.4
13	−723864	920418	723.6	−725203	919713	739.1
12	−736775	930423	755.6	−737776	930740	767.7
11	−737826	931570	756.0	−737776	930740	767.7
10	−738719	932874	754.3	−739528	932802	770.4
9	−741459	934817	765.3	−741177	935069	772.8
8	−743402	936656	762.5	−742855	937145	780.8
7	−744066	938107	785.3	−744532	939311	787.9
6	−745678	939910	781.8	−744532	939311	787.9
5	−746974	941101	790.8	−746348	941477	789.7
4	−750669	944516	799.2	−752217	943782	807.6
3	−757569	951627	829.5	−757317	950210	825.0
2	−759881	955427	832.4	−760740	954541	836.7
1	−769181	968037	846.9	−768495	969422	869.9
Average			769.6			777.9

with an accuracy that is comparable with the original resolution of the Argon imagery. The mosaic is a useful benchmark for comparing later changes in ice sheet geographical features, such as ice shelf margins, and for observing the changes in ice sheet dynamical features, such as ice streams. In a second paper, we show how a Bayesian boundary detection algorithm can be applied to the mosaic in order to extract the Antarctic coastline. The derived 1963 coastline can then be compared 8 with other similar measurements (Liu and Jezek 2004) to detect and measure coastal changes about the entire continent. 9

References

AMERICAN SOCIETY OF PHOTOGRAMMETRY, 1980, *Manual of Photogrammetry*, Fourth edition (Falls Church, VA: American Society of Photogrammetry).

BENTLEY, C.R., 1997, Rapid sea-level rise soon from West Antarctic Ice Sheet collapse? *Science*, **275**, pp. 1077–1078.

BINDSCHADLER, R.A., 1998, Monitoring ice sheet behavior from space. *Reviews of Geophysics*, **36**, pp. 79–104.

BINDSCHADLER, R.A. and SEIDER, W., 1998, Declassified intelligence satellite photography (DISP) coverage of Antarctica. *NASA Technical Memorandum-1998-206879*, Greenbelt, MD, pp. 37.

BINDSCHADLER, R.A. and VORNBERGER, P., 1998, Changes in the West Antarctic Ice Sheet since 1963 from declassified satellite photography. *Science*, **279**, pp. 689–692.

FAHNESTOCK, M., BINDSCHADLER, R., KWOK, R. and JEZEK, K.C., 1993, Greenland ice sheet surface properties and ice dynamics from ERS-1 SAR imagery. *Science*, **262**, pp. 1530–1534.

FERRIGNO, J.G., FOLEY, K.M., SWITHINBANK, C., WILLIAMS JR., R.S. and DALIDE, L.M., 2005, Coastal-change and glaciological map of the Ronne Ice Shelf area, Antarctica: 1974–2002. *Geologic Investigations Series Map I-2600-D*, U.S. Geological Survey.

FERRIGNO, J.G. and GOULD, W.G., 1987, Substantial changes in the coastline of Antarctica revealed by satellite imagery. *Polar Record*, **23**(146), pp. 577–583.

FERRIGNO, J.G., MULLINS, J.L., STAPLETON, J.A., CHAVEZ JR, P.S., VELASCO, M.G. and WILLIAMS JR, R.S., et al. 1996, Satellite image map of Antarctica. *Miscellaneous Investigations Map Series 1-2560*, U.S. Geological Survey.

Gray, A.L., Mattar, K.E., Vachon, P.W., Bindschadler, R., Jezek, K.C. and Forster, R., et al. 1998, InSAR results from the RADARSAT Antarctic Mapping Mission Data: Estimation of glacier motion using a simple registration procedure. In *Early Results from the First RADARSAT-1 Antarctic Mapping Mission*, K.C. Jezek, (Ed). (BPRC Technical Report 98-02), pp. 10–12.

Jezek, K.C., 1998, Flow variations of the Antarctic Ice Sheet from comparison of modern and historical satellite data. In *Geoscience and Remote Sensing Symposium Proceedings, IGARSS'98*, Seattle, WA (New York: IEEE International), **4**, pp. 2240–2242.

Jezek, K.C., 1999, Glaciological properties of the Antarctic Ice Sheet from Radarsat-1 synthetic aperture radar imagery. *Annals of Glaciology*, **29**, pp. 286–290.

Jezek, K.C. and Liu, H., 2005, Structure of Eastern Antarctic Peninsula ice shelves and ice tongues from synthetic aperture radar imagery. *Journal of Glaciology*, **51**, pp. 373–376.

Joughin, I. and Tulaczyk, S., 2002, Positive mass balance of the Ross Ice Streams, West Antarctica. *Science*, **295**, pp. 476–480.

Kim, K., 2004, Satellite mapping and automated feature extraction: GIS-based change detection of the Antarctic coast. PhD Thesis, Ohio State University, Columbus, OH.

Kim, K., Jezek, K.C. and Sohn, H., 2001, Ice shelf advance and retreat rates along the coast of Queen Maud Land, Antarctica. *Journal of Geophysical Research*, **106**(C4), pp. 7097–7106.

Koch, K.R., 1998, *Parameter estimation and hypothesis testing in linear models* (Berlin, New York: Springer-Verlag).

Kraus, K., 1993, *Photogrammetry, Volume 1: Fundamentals and Standard Processes*, Fourth edition (Bonn, Germany: Dümmler).

Liu, H. and Jezek, K.C., 2004, Automated extraction of coastline from satellite imagery by integrating Canny edge detection and locally adaptive thresholding methods. *International Journal of Remote Sensing*, **25**(5), pp. 937–958.

Liu, H., Jezek, K.C. and Li, B., 1999, Development of an Antarctic digital elevation model by integrating cartographic and remotely sensed data: a geographic information system based approach. *Journal of Geophysical Research*, **104**(B10), pp. 23199–23214.

Luchitta, B.K. and Ferguson, H.M., 1986, Antarctica: Measuring glacier velocities from satellite images. *Science*, **234**(4780), pp. 1105–1108.

McDonald, R.A., 1995, Corona: Success for space reconnaissance, a look into the cold war and a revolution in intelligence. *Photogrammetric Engineering and Remote Sensing*, **61**(6), pp. 689–720.

Merson, R.H., 1989, An AVHRR mosaic of Antarctica. *International Journal of Remote Sensing*, **10**, pp. 669–674.

Noltimier, K.F., Jezek, K.C., Sohn, H., Li, B., Liu, H. and Baumgartner, F., et al. 1999, Radarsat Antarctic mapping project – mosaic construction. In *Geoscience and Remote Sensing Symposium Proceedings, IGARSS'9*, Hamburg, Germany (New York: IEEE International), **5**, pp. 2349–2351.

Peebles, C., 1997, *The Corona Project: America's First Spy Satellites* (Annapolis, MD: Naval Institute Press).

Rignot, E., 2002, Ice-shelf changes in Pine Island Bay, Antarctica, 1947–2000. *Journal of Glaciology*, **48**(161), pp. 247–256.

Rott, H., Skvarca, P. and Nagler, T., 1996, Rapid collapase of northern Larsen Ice Shelf, Antarctica. *Science*, **271**, pp. 788–792.

Scambos, T.A., Hulbe, C., Fahnestock, M. and Bohlander, J., 2000, The link between climate warming and break-up of ice shelves in the Antarctic Peninsula. *Journal of Glaciology*, **46**(154), pp. 516–530.

Shepherd, A., Wingham, D.J., Mansley, J.A.D. and Corr, H.F.J., 2001, Inland thinning of Pine Island Glacier, West Antarctica. *Science*, **291**, pp. 862–864.

SKVARCA, P., RACK, W., ROTT, H. and IBARZABAL-DONANGELO, T., 1998, Evidence of recent climate warming on the Antarctic Peninsula. *Annals of Glaciology*, **27**, pp. 628–632.

STEARNS, L., 2002, The dynamic state of Whillans Ice Stream, West Antarctica. MS Thesis, Ohio State University, Columbus, OH.

STEARNS, L., JEZEK, K.C. and VAN DER VEEN, C.J., 2005, Decadal scale variations in ice flow along Whillans Ice Stream and its tributaries, West Antarctica. *Journal of Glaciology*, **51**(172), pp. 147–157.

SWITHINBANK, C. and LUCHITTA, B.K., 1986, Multispectral digital image mapping of Antarctic ice features. *Annals of Glaciology*, **8**, pp. 159–163.

SWITHINBANK, C., 1973, Higher resolution satellite pictures. *Polar Record*, **16**(104), pp. 739–751.

WHEELON, A.D., 1997, Corona: The first reconnaissance satellites. *Physics Today*, **50**(2), pp. 24–30.

WILLIAMS JR, R.S., FERRIGNO, J.G., SWITHINBANK, C., LUCHITTA, B.K. and SEEKINS, B.A., 1995, Coastal change and glaciological maps of Antarctica. *Annals of Glaciology*, **21**, pp. 284–290.

WINGHAM, D.J., RIDOUT, A.J., SCHARROO, R., ARTHERN, R.J. and SHUM, C.K., 1998, Antarctic elevation change from 1992 to 1996. *Science*, **282**, pp. 456–458.

ZHOU, G. and JEZEK, K.C., 2002, Satellite photograph mosaics of Greenland from the 1960s era. *International Journal of Remote Sensing*, **23**(6), pp. 1143–1159.

ZHOU, G., JEZEK, K.C., WRIGHT, W. and GRANGER, J., 2002, Orthorectification of 1960s satellite photographs covering Greenland. *IEEE Transactions on Geoscience and Remote Sensing*, **40**(6), pp. 1247–1259.